Structural Engineering and Mechanics, *Vol. 75, No. 6 (2020) 723-736*
DOI: https://doi.org/10.12989/sem.2020.75.6.723

Acoustic emission technique to identify stress corrosion cracking damage

V. Soltangharaei[1a], J.W. Hill[1], Li Ai[1], R. Anay[1], B. Greer[2b], M. Bayat[*1] and P. Ziehl[1c]

[1]*Department of Civil and Environmental Engineering, University of South Carolina, Columbia, SC, USA*
[2]*Senior Technical Leader, Electrical Power Research Institute, USA*

(Received March 13, 2020, Revised April 7, 2020, Accepted April 14, 2020)

Abstract. In this paper, acoustic emission (AE) and pattern recognition are utilized to identify the AE signal signatures caused by propagation of stress corrosion cracking (SCC) in a 304 stainless steel plate. The surface of the plate is under almost uniform tensile stress at a notch. A corrosive environment is provided by exposing the notch to a solution of 1% Potassium Tetrathionate by weight. The Global b-value indicated an occurrence of the first visible crack and damage stages during the SCC. Furthermore, a method based on linear regression has been developed for damage identification using AE data.

Keywords: acoustic emission; damage identification; global b-value; pattern recognition; stress corrosion cracking

1. Introduction

A majority of the nuclear power plants in operation in the United States of America (USA), were built in the 1960s, 1970s, and 1980s, and they have made a large contribution to the generation of the power used in this country (Hill 2018). Despite the large energy contribution of nuclear power plants in the US, they have several disadvantages. Nuclear power plants are required to meet high-level safety standards. In addition, they face the challenge of the safe containment of spent fuel byproducts, which must be continually reassessed to prevent environmental release. The current long-term plan for spent nuclear fuel is geological repositories. There are two temporary alternatives to preserve the spent nuclear fuel until the long-term facilities are constructed. They are cooling pools and dry cask storage systems (DCSS). DCSSs have been utilized since the 1970s and 1980s (Hill 2018). The stainless-steel canisters encase the used fuel and high-level waste in an environment which is filled by an inert gas. DCSSs are sealed by welding and protected by an external reinforced concrete overpack to avert any potential radiation transmission to humans. The welding on the storage containers causes austenitic materials to become sensitized when Carbon settles between intergranular boundaries and causes chromium carbide precipitation, which removes the chromium from the intergranular boundaries. This reaction makes steel more susceptible to SCC. In coastal region where there is high humidity, there is greater potential for the environmental conditions to be conducive to the degradation of the DCSSs.

Many DCSSs were initially licensed for a 20-year operation. At this point in time, many of the original licenses are approaching expiration (Hill 2018). The licenses can only be extended through inspections to verify the structural operability for a desired future time frame. One traditional method is visual inspection. The visual inspection of the DCSSs is time-consuming, expensive, subjective, and challenging due to limited access to the surface while stored inside the concrete overpack. Many researches have been done also on the numerical modeling of structures to capture and considering their damage and preparing a damage model (Mahdavi *et al*. 2019, Bayat *et al*. 2019, Khorshidi *et al*. 2014, Ahmadi *et al*. 2018, Ahmadi *et al*. 2105, Bayat *et al*. 2019, Dastjerdi *et al*. 2018, Gholizadeh *et al*. 2015, Hakan 2008, Kainuma *et al*. 2018, Mirfakhraei *et al*. 2020).

Acoustic emission is proposed as an alternative method to identify and quantify damages caused by stress corrosion cracking (SCC). Acoustic emission (AE) is a structural health monitoring technique. This method is very sensitive, nondestructive, and has an ability for continuous monitoring. It has already been utilized for the identification of damage in reinforced concrete structures affected by alkaline silica reaction (Soltangharaei *et al*. 2018), cement paste (Soltangharaei *et al*. 2018), and concrete structures under loading (Forde *et al*. 2016). Moreover, it has been used for the health monitoring of steel structures such as steel bridges (Holford *et al*. 2001, Roberts and Talebzadeh 2003, Yu *et al*. 2011).

Several researchers have investigated different types of corrosion using AE (Mazille *et al*. 1995, Fregonese *et al*. 2001, Kim *et al*. 2003, Shaikh *et al*. 2007, Alvarez *et al*. 2008, Lee *et al*. 2008, Calabrese *et al*. 2010, Jirarungsatian and Prateepasen 2010, Du *et al*. 2011, Xu *et al*. 2011, Xu *et al*. 2012, Xu *et al*. 2013, Hwang *et al*. 2015, Kovač *et al*. 2015, Wu *et al*. 2015, Morizet *et al*. 2016). Xu *et al*. (2011) investigated pitting corrosion in 304 stainless with various PH values using AE. They found that the main AE source was bubble formation and more AE activities were emitted

∗Corresponding author, Mahmoud Bayat
E-mail: mbayat14@yahoo.com; mbayat@mailbox.sc.edu
[a] Postdoctoral Fellow
E-mail: vafa@email.sc.edu
[b] B. Geer
E-mail: bgreer@epri.com
[c] Professor
E-mail: ziehl@cec.sc.edu

ISSN: 1225-4568 (Print), 1598-6217 (Online)

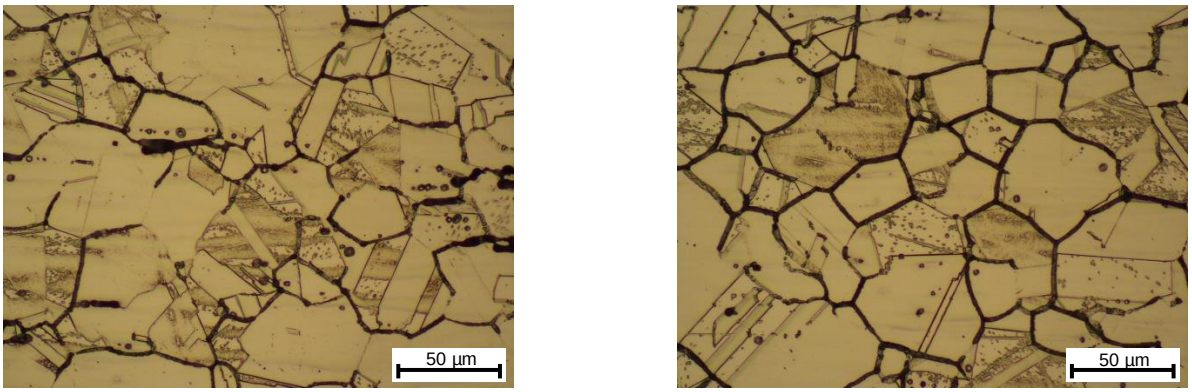

(a) Sensitization after 2 hours (b) Sensitization after 14 hours

Fig. 1 Metallography during sensitization process at 500 times magnification

from a specimen exposed to a lower concentration solution. Mazille *et al*. (1995) also utilized AE technique to investigative pitting corrosion in AISI 316L austenitic stainless steel. They found that the corrosion rate has a correlation with AE data. Fregonese *et al*. (2001) studied the development of pitting corrosion in AISI 316L austenitic stainless steel by using AE technique. They observed that the AE activity shows the development of the pits in the form of occluded cells, and there were not significant AE activities at the initial stage of corrosion. Jirarungsatian *et al*. (2010) proposed to use the duration and frequency of AE signals to classify the data emitted from pitting and uniform corrosion process.

Some researchers have focused on SCC (Shaikh *et al*. 2007, Alvarez *et al*. 2008, Du *et al*. 2011, Xu *et al*. 2012, Kovač *et al*. 2015). Xu *et al*. (2012) utilized acoustic emission to study stress corrosion cracking in 304 stainless steel during constant load and in a high-temperature aqueous environment. They attributed the high amplitude signals to the crack propagation and the low amplitude signals to plastic deformations. They (Xu *et al*. 2013) also found that the fracture mode for stress corrosion cracks in the sensitized 304 stainless steel was a combination of intergranular and transgranular cracking. Alvarez *et al*. (2008) studied the AE signals generated by transgranular and intergranular SCC in sensitized type AISI 304 stainless steel samples. They observed that the AE activities during the propagation of transgranular SCC is much higher than the AE activity during the intergranular SCC. Du *et al*. (2011) studied the corrosion of 304 stainless steel in an acidic NaCl solution during a slow strain rate tensile test using the electrochemical noise and acoustic emission techniques. The AE data was classified according to their frequency distributions. The signals with a frequency between 250 to 320 kHz were recognized as the cracking signals. Shaikh *et al*. (2007) evaluated stress corrosion cracking of AISI type 316LN stainless steel using AE. They observed that AE was continuous before crack initiation and AE rate decreased after crack initiation and propagation.

In this study, unsupervised pattern recognition was conducted by using frequency-energy based features. A source location algorithm was employed to verify the AE sources. Furthermore, the resulting clusters were localized to identify the AE signal signatures caused by SCC under constant bending stress in a stainless-steel plate. Incremental and Global b-value analyses were conducted for damage identification and quantification during the SCC. A method based on linear regression is proposed as a damage quantification and identification index. This study is an initial part of the project for damage detection and quantification of DCSSs affected by SCC to evaluate the structural qualification for license extension.

2. Test setup and experimental procedure

A 304H stainless steel plate was prepared and sensitized for an SCC test. In many nuclear applications, 304 L stainless steel is used, however 304H stainless steel was tested in this paper due to the higher carbon content of the material which would mean a faster sensitization process leading to a shorter heat treatment duration. The steel plate was 305 mm (12 inches) by 311 mm (12.25 inches) and 16 mm (0.625 inches) thick. The sensitization process was conducted by exposing the steel plates to a temperature of 675^{o}C (1250^{o}F) for 14 hours in a vacuum furnace. The carbon in the material bonds with chromium and forms carbides in the grain boundaries, this reduces the concentration of chromium near the grain boundaries and makes the steel more susceptible to intergranular SCC. The metallographic pictures of the sensitization process after 2 hours and at the completion of the process (14 hours) are presented in Fig. 1.

A stress concentrating starter notch with the dimensions of 12 mm (0.5 in) in length, 0.5 mm (0.02 in) in width, and 1 mm (0.04 in) in depth was produced in the plate by using electrical discharge machining (EDM).

The specimen was fabricated with two perpendicular tabs, welded to the bottom face of the specimens with a hole located 76 mm (3 inches) from the bottom face of the plate. A 19 mm (0.75 in) bolt with a nut was inserted inside the hole and tightened to apply a compressive force to the welded tabs. This compressive force created a bending moment in the specimens and tension on the surface of the plates, thereby exerting stress in the notch. The location of the applied force is shown in Fig. 2. The goal for this study is stress corrosion crack propagation under the elastic region of mechanical behavior of stainless steel in a

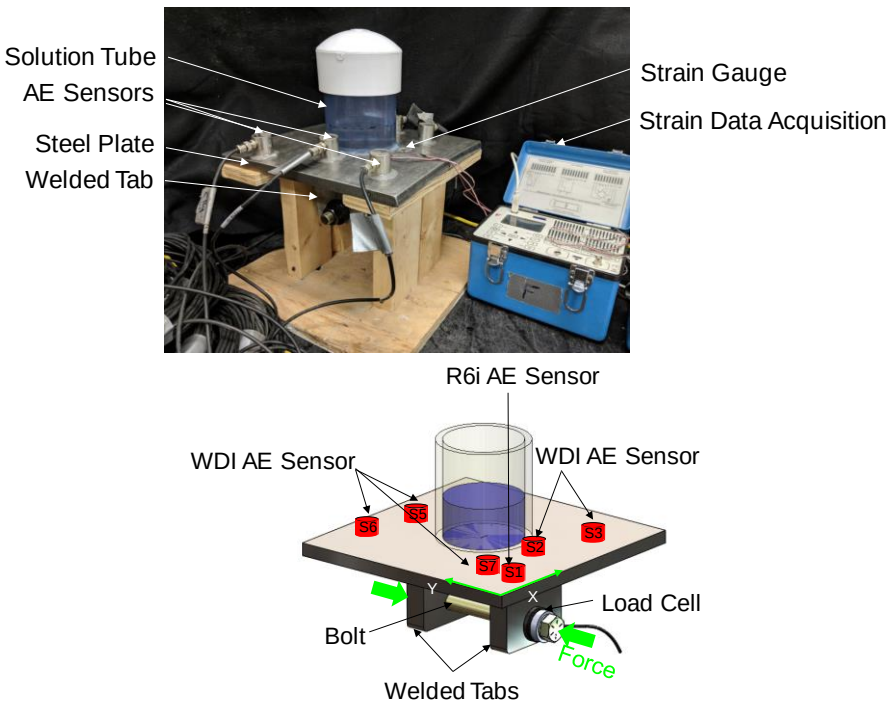

Fig. 2 Test Setup

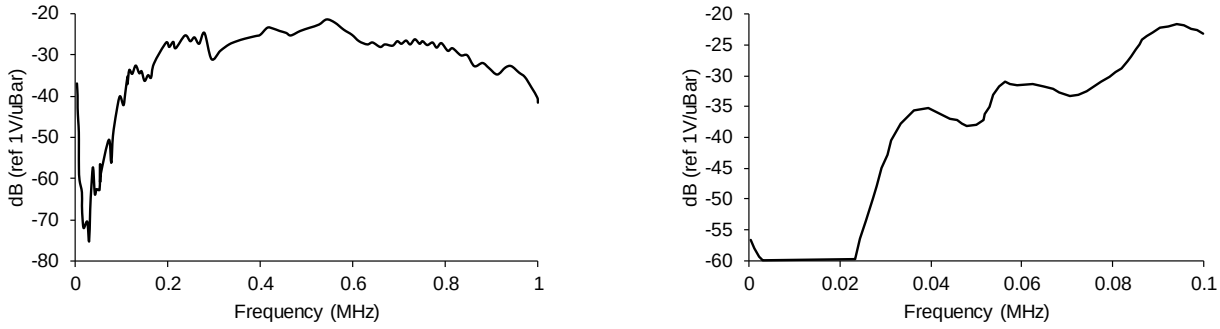

(a) WDI sensors (b) R6I

Fig. 3 Sensitivity curves (MISTRASGroup 2011a and b)

reasonable period. Therefore, the compressive force applied to the bolt was calculated in a way that the tensile stress on the top surface of the plate at the notch location was less than the yielding stress of the 304H stainless steel (206 MPa) Moreover, the stress on the top surface should be large enough for crack propagation in a reasonable time frame. Therefore, the target stress was set at 186 MPa, which was the 90% of the yielding stress. Two strain gauges (Micro-Measurements 2A-06-250LW-350) were attached on the surface of the plates along the bending axis to prevent the tensile strain on the surface from exceeding the corresponding strain value for the defined target stress. The strain data was recorded by a P3 Strain Indicator and Recorder manufactured by Micro Measurements. The required torque value for fastening the bolt was calculated and applied. The test setup is shown in Fig. 2.

A 1% potassium tetrathionate ($K_2S_4O_6$) solution was used as an electrolyte to provide a corrosive environment for the test. In addition, sulfuric acid was utilized to reduce the solution's pH to 3.0, to expedite the corrosion reaction. The solution was placed in a tube container, which was attached with silicone on the surface of the plate in the middle region of the plate. Six WDI-AST wideband AE sensors with a frequency response of 200-900 kHz and two resonant R6I-AST AE sensors with a frequency response range of 40-100 kHz were attached on the surface of a steel plate by using epoxy. The WDI sensors have a peak sensitivity of -25 dB with the reference of V/µbar. The sensors have the dimensions of 29 mm (diameter) and 30 mm (height). The R6I sensors have a peak sensitivity of -23 dB with the reference of V/µbar and the dimensions of 29 mm (diameter) and 40 mm (height). Both wideband and resonant sensors have internal preamplifiers with 40 dB gain. The sensitivity curves for the sensors are presented in Fig. 3.

A 16-channel DiSP system manufactured by MISTRAS Group, Inc. (Princeton Junction, New Jersey) was utilized for a data acquisition. After attaching the sensors on the specimen and connecting them to the data acquisition, a background noise test was conducted for 24 hours to

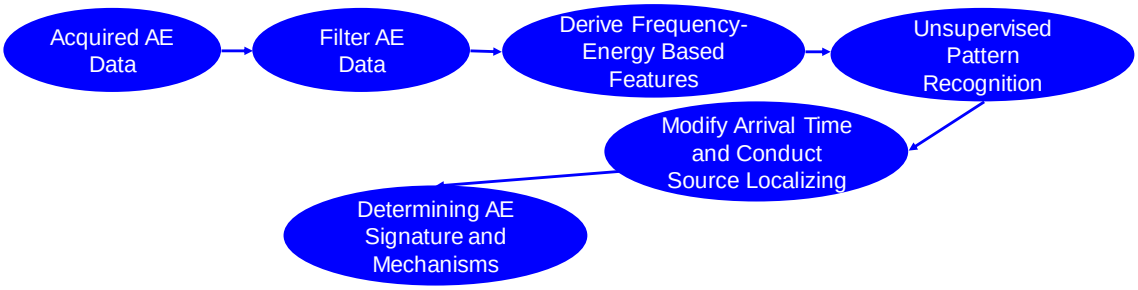

Fig. 4 Data analysis procedure

determine the noise level in the testing environment. Therefore, the amplitude threshold was set to 32 dB in the data acquisition system according to the background noise test to avoid any potential environmental noise signal. The sampling rate for the system was set to 1 MHz. The pre-trigger time, which is the time before the first threshold crossing of a signal that an AE system recovers data, was set to 256 μs. This timing parameter is set to make sure; the recording system does not miss the time attributed to signal initiation. The time for terminating the measurement of the AE signals, also known as hit definition time (HDT), was set to 400 μs. A signal started to be recorded at the moment that its voltage first exceeds the set threshold, and the recording is stopped when an amount of time equal to HDT has passed without any threshold crossings. The peak definition time (PDF), which is utilized to find the peak in a signal, was set to 200 μs. In other words, this parameter gives some control over which peaks are used for calculating rise time and amplitudes, when a signal has several peaks. The hit lock time (HLT) is the time at the end of a signal to prevent any reflections, was set to 200 μs. HLT is a time which any threshold crossing happening during this time will not be included in a hit waveform (MISTRASGroup (2014)). The sensitivity of external sensors and calibration of channels were conducted by applying Hsu-Nielsen sources before starting the test (Hsu 1981).

The specimen was tested for 19 days. The test was monitored frequently for preventing any potentiation abnormality in the progression of the test. Visual inspection of the plate was also conducted regularly every 1-3 days using microscopic and digital large-scale photographs. A Dino-Lite digital microscope with maximum magnification of 184X was utilized for taking the microscopic pictures. The solution and tube were removed for taking pictures and checking the status of crack formation and extension. The test was continued by replacing the solution and tube on the surface.

3. Data analysis method

The steel plate was continuously monitored for 19 days. The AE data was initially filtered to delete suspicious and non-genuine data. Then, unsupervised pattern recognition was conducted on the data acquired by the broadband sensors considering the frequency-energy based features. The classified data was localized using an interactive source location algorithm and modified time of arrival (TOA) of the events. Signal signatures for stress corrosion cracking were developed. The procedure is shown in Fig. 4.

Furthermore, Incremental and Global b-value procedures were utilized for damage identification and quantification. A method based on b-value was developed to identify the damage stages during stress corrosion cracking. The analysis procedure is described in the following subsections.

3.1 Filtering AE data

The AE data contained extraneous signals in some channels due to faulty connections, and these were filtered according to the difference between genuine and false AE signals. Examples are shown in Fig. 5. Different filtering approaches were taken for AE data collected by broadband and resonant sensors since the noise level in the two types of sensors were different due to sensitivity and frequency response ranges. The false data has a much lower counts compared to the genuine data. Therefore, this feature was considered as the main criterion for filtering the data in this study. For broadband sensors, the AE data with counts to peak less than 18 were deleted. For resonant sensors, the AE signals with counts less than 10 were initially removed from the data. Then the AE signals with signal strength less than 10,000 pVs and duration less than 300 μs were deleted. The waveforms of the filtered data were visually observed for further filtering. For the source location and pattern recognition purposes, only the AE events containing more than three hits were considered.

3.2 Feature extraction and unsupervised pattern recognition

The AE signals were transferred to the frequency domain by using the Fast Fourier Transform (FFT). The Nyquist frequency was divided by ten equal frequency bands. The area enclosed in each frequency band under the FFT spectrum was calculated and normalized to the total signal energy. The resulting values were considered as the frequency-energy based features. Therefore, each signal originally had ten frequency-energy based features. To classify the data, it is usually better to reduce the number of features or delete the features with the highest correlation. Principal Component Analysis (PCA) was employed to reduce the redundancy in the data features and transfer the data to a new coordinate. In the PCA, the eigenvalue

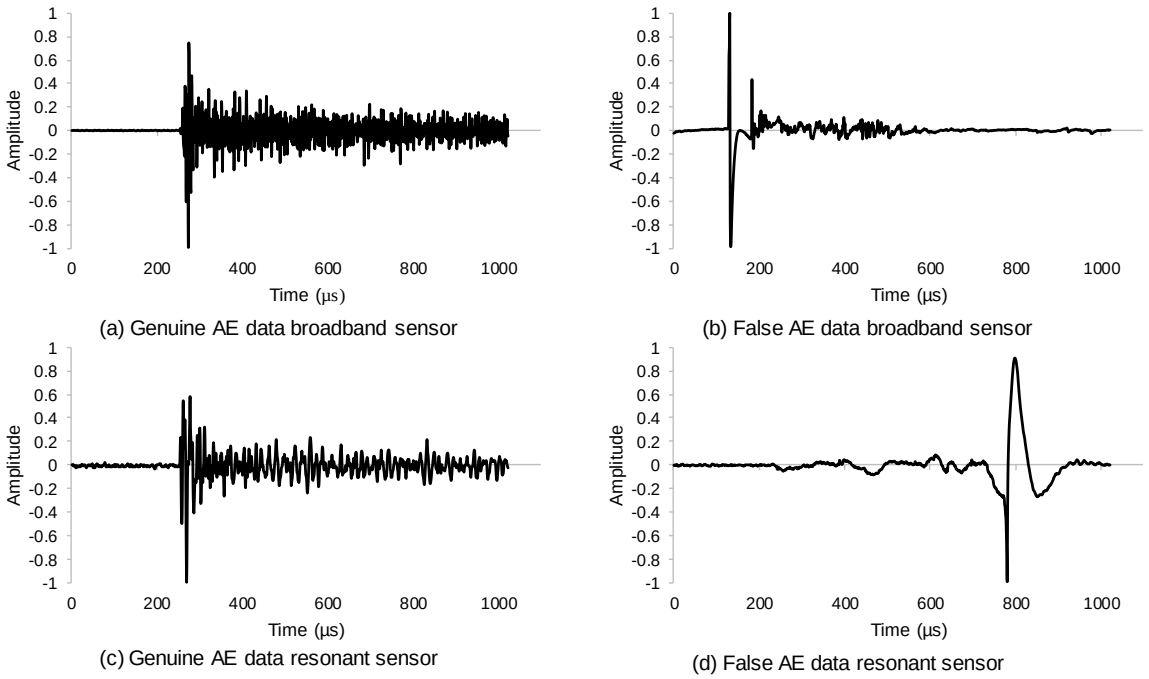

Fig. 5 Genuine and extraneous AE data

analysis was conducted on the covariance matrix of AE data with frequency-energy based features. The resulted eigenvectors were principal components (PC). Eigenvalues attributed to each principal component were descending sorted and normalized to the total value.

The principal components with the highest percentage of eigenvalues were selected as an input matrix for the classifier. In this study, the first four principal components were selected to represent 93% of the information in the AE data with the original frequency-energy based features. In other words, the first four principal components accounted for 93% of variance in the data set. Therefore, the first four principal components were considered as the data features, and an input matrix for clustering algorithm included AE signals with four PCs (four features). An agglomerative hierarchical algorithm (Tan *et al*. 2018) was used as an unsupervised pattern recognition method for classifying the AE data. The algorithm calculated the Euclidian distances between the input features for all observations (AE signals). The result was presented as a proximity matrix. The data was linked in pairs according to the calculated distances in the proximity matrix and Ward's method (Murtagh and Legendre 2014). The results were the new groups of data, which were called "objects". The same procedure was repeated and new groups were merged until, at the end, a single cluster including all data was formed. The more detailed information about feature extraction and pattern recognition methods are presented in (Soltangharaei *et al*. 2018).

3.3 Continuous wavelet transform

To better present the signal signatures in terms of time and frequency, the continuous wavelet transform (CWT) was utilized. CWT presents the time series in a high time resolution for the high-frequency components and a high-frequency resolution for the low-frequency components (Suzuki *et al*. 1996). The CWT was calculated using the following equation:

$$CWT(a,b) = \int S(t) * |a|^{-0.5} \Psi\left(\frac{t-b}{a}\right) dt \quad (1)$$

Where a is the scale parameter and controls the frequency calculation of a signal, and b is the shift parameter, which controls the movement of wavelets through the signal in the time domain. *S(t)* is a time history signal. The wavelet coefficients are calculated by convolution of wavelets through a signal. The second part of the Eq. (1) ($\Psi_{a,b}(t) = |a|^{-0.5}\Psi\left(\frac{t-b}{a}\right)$) refers to the wavelets. The mother wavelet in this study is a Gabor wavelet, which is based on a Gaussian function (Suzuki *et al*. 1996). The CWT was conducted using AGU-Vallen Wavelet Software produced by the Vallen Systeme Company.

3.4 Modification of TOA and source location algorithm

An iterative algorithm was coded and utilized for estimating the source locations of AE data recorded during the experiment. Before applying the algorithm on the data, new travel times for the signals were calculated using the Akaike Information Criterion (AIC) for a better estimation of motion initiations (Akaike 1998, Carpinteri *et al*. 2012). The AICs of the signals were calculated by using the following equation (Carpinteri *et al*. 2012):

$$AIC(t_w) = t_w \log\left(\sigma^2\left(S(1\ to\ t_w)\right)\right) + (n_w - k_w)\log\left(\sigma^2\left(S\left((1+t_w)\ to\ n_w\right)\right)\right) \quad (2)$$

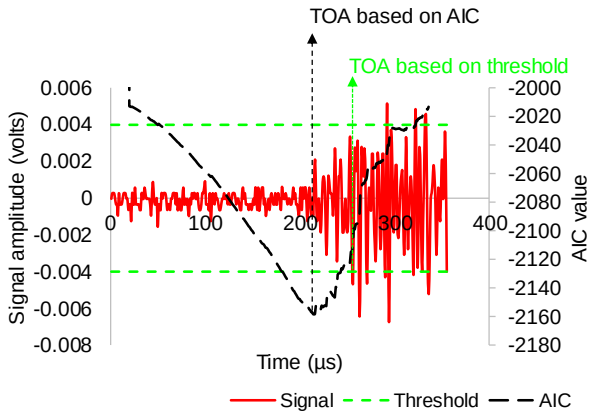

Fig. 6 Time of arrival calculation

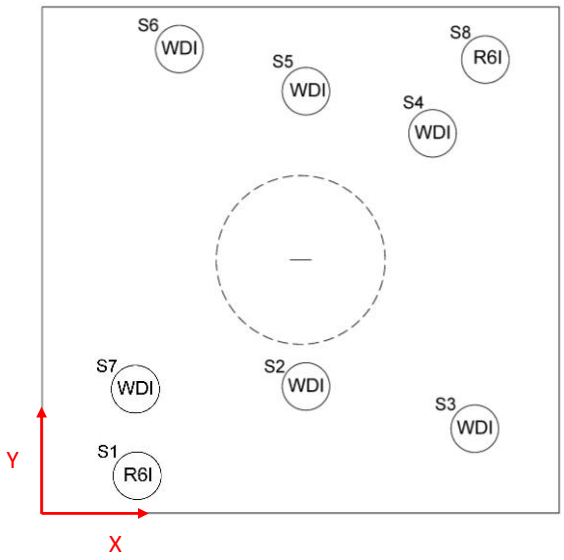

Fig. 7 Sensor layout

The equation is referred to as "AIC-picker". A windowed section of a signal, which contains signal initiation, is usually considered for AIC calculation. The last point of the windowed signal is denoted by n_w and S is the signal amplitude values. t_w is the times in the windowed signal, which ranges from 1 to n_w. $\sigma^2(S(1\ to\ t_w))$ is the variance of signal voltages from the beginning of the signal to the desired time (tw) and $\sigma^2\left(S((1+t_w)\ to\ n_w)\right)$ is the variance of signal voltages from tw+1 to n_w. The minimum AIC values show an initiation of p-wave.

Most of the AE data recorded during stress corrosion cracking tests were weak. Therefore, the threshold method did not show the real TOAs of the signals. AIC was used in this study to calculate the more realistic TOAs of signals to improve the source location results. An example of a signal is presented in Fig. 6. As seen in the figure, the threshold could not capture the TOA of the signal because the initial part of the signal is very weak and falls below the threshold.

After modification of the TOAs, the resulting values were used for source location. The sensor layout is shown in Fig. 7. The sensors are labeled from S1 to S8. The sensor types are written inside the circles.

Table 1 Sensor coordinates

Sensor	X (mm)	Y (mm)
S1	57	25
S2	159	76
S3	262	51
S4	235	229
S5	159	254
S6	83	279
S7	57	76
S8	267	274

The coordinates of the sensors are presented in Table 1.

A source location algorithm was coded to minimize the difference between observed and calculated TOAs (Ge 2003). The least-squares method was used for optimization (Dennis Jr 1978)

A second derivative of AIC (Eq. 2) (Maeda 1985, Carpinteri *et al*. 2012) was utilized to select the best signals for the source location. The equation (Carpinteri *et al*. 2012) is as follows:

$$DD = (AIC(t_{min} - \delta t) + AIC(t_{min} + \delta t) - 2AIC(t_{min}))/\delta t^2 \quad (3)$$

where t_{min} is the time in a signal corresponding to the minimum AIC (TOA). δt is the small time interval, which is considered before and after t_{min} for the calculation of *DD* (Carpinteri *et al*. 2012). In this study δt is assumed to be 15 µs. The first four or three largest DD for each event were selected for the source location.

3.5 b-value analysis

b-value analysis is a method based on Gutenberg-Richter equation (Rao and Lakshmi 2005) in the seismology field, which indicates the occurrence frequency versus magnitudes of earthquakes in one region. It states that earthquakes with large magnitudes occur less frequently. A similar concept has been utilized in acoustic emission, and the Gutenberg-Richter equation was modified ((Rao and Lakshmi 2005)) as follows:

$$LogN = a - b(\frac{A}{20}) \quad (4)$$

where N is the number of AE hits with amplitudes more than A. The AE signals with larger amplitudes are expected to be less frequent than the signals with the lower amplitudes. The relationship between the *logN* and amplitude (A) is linear or close to linear. Therefore, linear regression is used to calculate a and b. The smaller b-values show a higher chance of damage.

In this study, two approaches were considered for b-value calculation. The first approach is named "Incremental b-value". In this method, the whole data (hits) was divided by the desired increments and b-values were calculated in each increment. N in Eq. (4) for the Incremental b-value is the number of AE hits with amplitudes more than A in each increment.

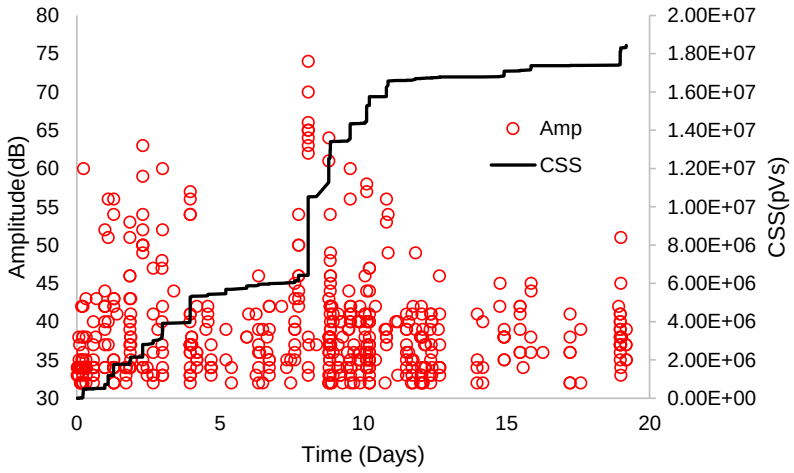

Fig. 8 Filtered AE data

(a) At 0 day

(b) At 6 days

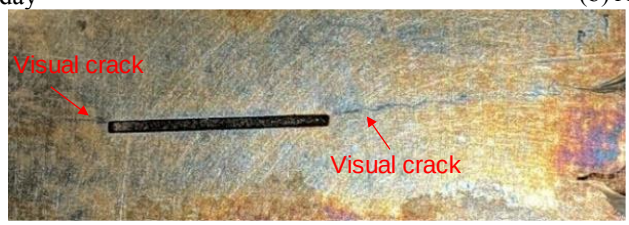

(c) At 19 days

Fig. 9 Photos of the notch at different test days

The second approach is named "Global b-value". In this method, the b-values were calculated by considering all data from the beginning of the test to the desired experiment times. *N* in Eq. (4) in the Global b-value is the number of AE hits with amplitudes more than *A*, which is calculated by considering all AE data from the beginning of test to a desired monitoring time.

Furthermore, the R^2-value associated with each Global b-value was also calculated using the following equation:

$$R^2 = 1 - \frac{\sum_{i=1}^{n}(\hat{y}_i - y_i)^2}{\sum_{i=1}^{n}(y_i - \bar{y})^2} \quad (5)$$

where $\hat{y}_i$ is the estimated value of *logN* for an i^{th} point by using the fitted line and y_i is the real value of *logN* for the i^{th} point. $\bar{y}$ is the average value of *logN*. Index *n* denotes the last desired data to calculate the b-value.

The modified version of b-value was also developed by using signal strength instead of amplitude. The relationship between *log(Signal Strength)* and *logN* was not linear. Therefore, the relationship between *log(Signal Strength)* and *N* was considered. The relationship resulted in a bi-linear behavior. The *R^2-values* were also calculated by considering the *log(Signal Strength)* and *N* relationship.

4. Results and discussion

The AE data was filtered according to the procedure described in section 3.1. The filtered AE data for both resonant and broadband sensors were shown in Fig. 8. Both amplitude and cumulative signal strength (CSS) are illustrated in the figure. There is a big jump in the CSS curve around the 8^{th} day. Moreover, smaller jumps in the CSS curve can be observed earlier than that. The sudden increase in the CSS curve is usually attributed to crack formation or damage progression.

The steel plate was visually inspected. The pictures were taken at 0 (prior to the experiment), 6, and 19 days after initiation of the experiment as shown in Fig. 9. No visible crack was observed before the 6^{th} day of the experiment, whereas some AE events were recorded during the first six days. The first visible crack was observed at 9 days of the test as shown in Fig. 10. A major jump in CSS was observed at around 8 days, which approximately coincides with the occurrence of the first visible crack. The events during this jump can be attributed to macro-crack initiation during the SCC process.

A visible crack (macro-crack) was observed along the central (the tensile) axis of the plate after 19 days (Fig. 9

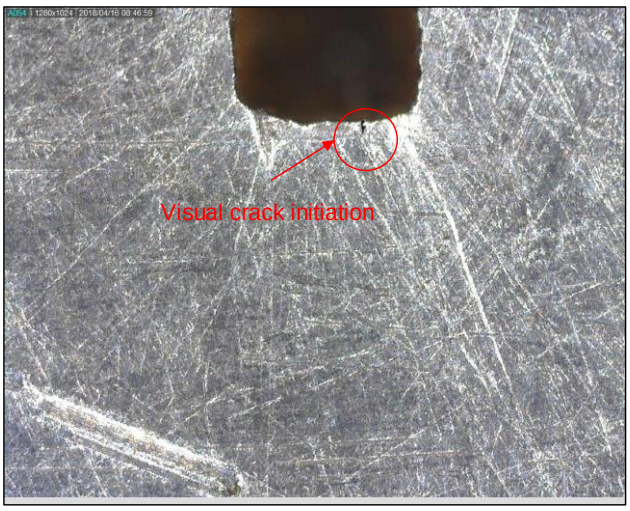

(a) At 9 days

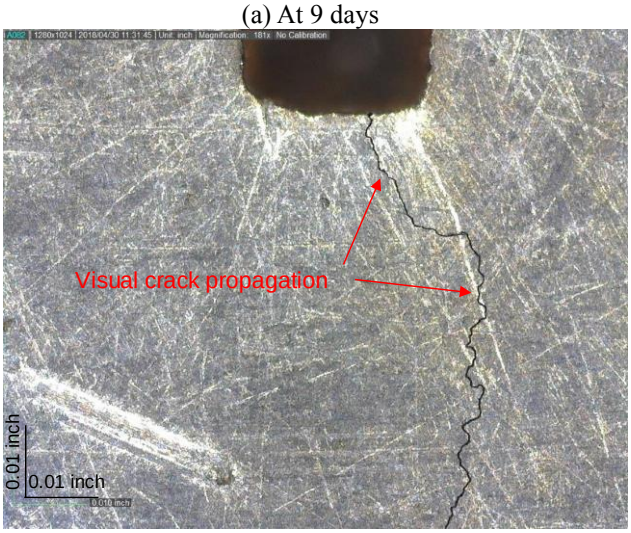

(b) At 19 days

Fig. 10 Microscopic pictures of the notch

and Fig. 10). It measured approximately 50.8 mm (2 inches) in length, which included cracks on either side of the notch. The crack width was measured using microscopic pictures and proved to be a maximum of 11.6 µm wide at the edge of the notch and 9.5 µm at the widest part of the crack.

4.1 Pattern recognition and signal signatures

The AE data was classified by using an agglomerative hierarchical algorithm and frequency-energy features as described in section 3.2. The dendrogram and the data presentation in the principal components (PC) are shown in Fig. 11. The data was grouped by upside-down U-shaped links as shown in the dendrogram, and the height differences between the branches show the distance between the merged data sets. The vertical axis in Fig. 11a presents the link heights calculated by using Euclidian distance and Wards algorithm as described in section 3.2. The vertical axis of Fig. 11a is unitless, since the original features used in the PCA and unsupervised pattern recognition algorithm were normalized. The values on the horizontal axis in Fig. 11a are the labels related to the original data and the subsets that resulted from the original data. The data was classified into three clusters (Cluster 1, Cluster 2, and Cluster 3). The red line depicts the desired cluster level in the data. Moreover, the data are presented in the PC space as shown in Fig. 11b. The corresponding values for each dot do not have any unit due to the reason mentioned earlier.

The frequency-energy distributions of AE signals for the three clusters are shown in Fig. 12a. Cluster 1 has the highest energy contribution (29%) in the frequency band of 0-100 kHz among the clusters. However, the energy distribution in this cluster looks uniform at the other frequencies. Cluster 2 has 45% of its energy in the frequency range of 100-200 kHz. Cluster 3 has 45% of its energy in the frequency range of 150-300 kHz. Average values of parametric features for the hits of each cluster have also been shown in Fig. 12b. In the figure, “Time” refers to the average TOAs for the hits. The times of occurrence of hits attributed to a specific cluster were averaged and presented as “Time” in the figure. In other words, “Time” in Fig. 12b indicates the distribution of AE data for each cluster in terms of monitoring time (19 days). Accordingly, the signals in Cluster 1 and 3 appear averagely later than Cluster 2 as seen in Fig. 12b.

Rise Time refers to the time from signal initiation to the time corresponding to the maximum signal amplitude. Counts to peak is referred to the number of signal crossing with the threshold, calculated from signal initiation to the maximum signal amplitude. Counts is the number of signal crossing with the threshold through the entire signal. Duration is referred to the time that signal voltages exceed the threshold. Amplitude is referred as the maximum voltage value in a signal, shown either as voltage or dB (Decibel). Signal strength is mathematically defined as the integral of the rectified voltage signal over the signal duration. The average signal strength of Cluster 3 is much more than the two others. The large signal strength values of Cluster 3 are mainly due to its large duration rather than its large amplitude as shown in Fig. 12b. Frequency Centroid is resulted from calculating the geometric centroid of area under FFT spectrum. Peak Frequency is the frequency attributed to the maximum FFT magnitude for a signal. RA value (Rise Angle) is the ratio of risetime to amplitude, which has the lowest average value for Cluster 1and the largest for Cluster 2.

The results of the classification are presented in terms of amplitude and CSS for the three clusters in Fig. 13. As seen, Cluster 3 contributes to a large portion of acoustic emission energy released during the SCC process. This was previously observed in the average CSS of this cluster in Fig. 12b. As mentioned, a significant jump in CSS occurred at 8 days, which is close to the time when the first visible crack was observed. The jump is caused by Cluster 3 (green color) as seen in Fig. 13.

Source location was conducted by determining TOAs of the hits using AIC and choosing the best hits for source location according the procedure outlined in section 3.3. The results are presented in Fig. 14 at the experiment times of 4 days, 9 days, and 19 days. The located events were indicated according to the assigned clusters. Small black

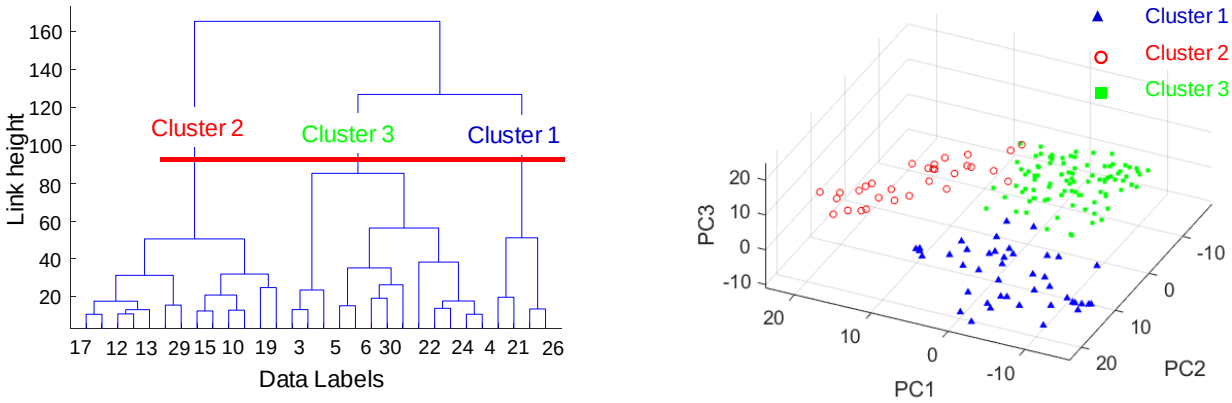

(a) Dendrogram (b) PCA result

Fig. 11 Cluster results

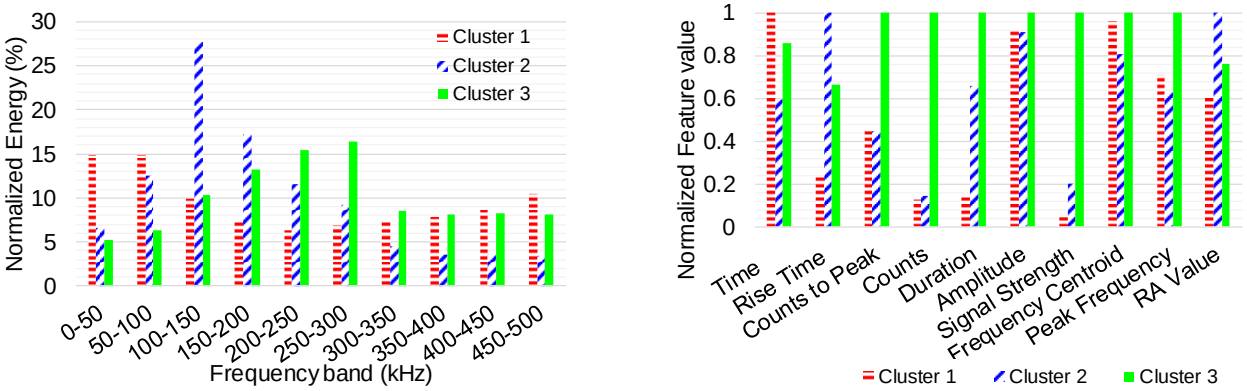

(a) (b)

Fig. 12 (a) Average energy distribution of data in frequency domain; (b) Normalized AE parametric features

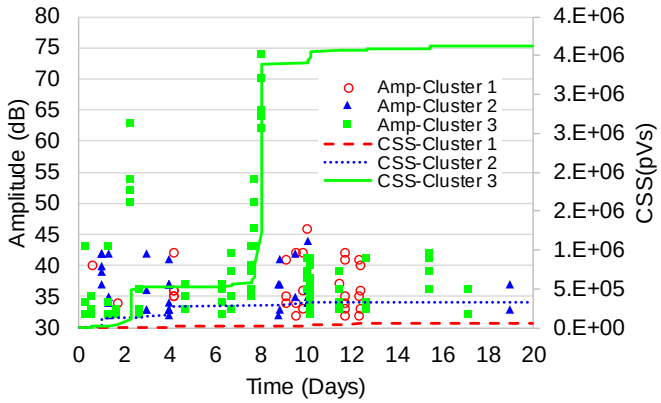

Fig. 13 Amplitude and CSS versus time for classified

circles indicate the sensors and their labels are shown next to the sensors. The sensor types (broadband (WDI) and resonant (R6I)) are labeled. The large circle with a dashed line indicates the location of the solution tube. The visual crack is also presented in Fig. 14c. The region inside the data large circle was exposed to the corrosive condition. Therefore, it can be concluded that the AE events located inside the circle have a high chance of being related to the SCC. The first visible crack was observed at the 9th experiment day. However, there are several events located before that time around the notch as seen in Fig. 14. This supports the observation that AE is sensitive and capable of capturing the hits attributed to microcracks caused by SCC (before a visible defect appears). The percentage of the events for Cluster 3 increases during the experiment. The percentages of events for Cluster 3 are 33%, 46%, and 57% for 4 days, 9 days, and 19 days, respectively. Therefore, most located events are from Cluster 3. As seen in Fig. 14b, the event (green square point) at the right site of the notch appeared at the time close to the 9th day, when the first visible crack was observed in the same location. This event is from Cluster 3.

An example of signals for each cluster is shown as the waveforms and wavelet contours in Fig. 15. All the signals in Fig. 15 are normalized to their maximum amplitudes to show their waveforms clearly. However, the wavelet coefficients are scaled to the maximum coefficient, which is related to the signal in Cluster 3 (Fig. 15c) to show the energy levels of the signals. The signals in Cluster 3 have a large energy concentration (between 200 to 300 kHz) as shown in Fig. 15c. They have larger durations and signal strength compared to the other clusters. They have the largest acoustic emission energy contribution during the SCC process and their AE energy contribution significantly increases around an occurrence of the first visible crack. Furthermore, an event from Cluster 3 occurred at the location of the first visible crack and in the time close to the 9th day when the first visible crack was observed. Therefore, the signals in Cluster 3 may be mainly associated with the macrocrack formation.

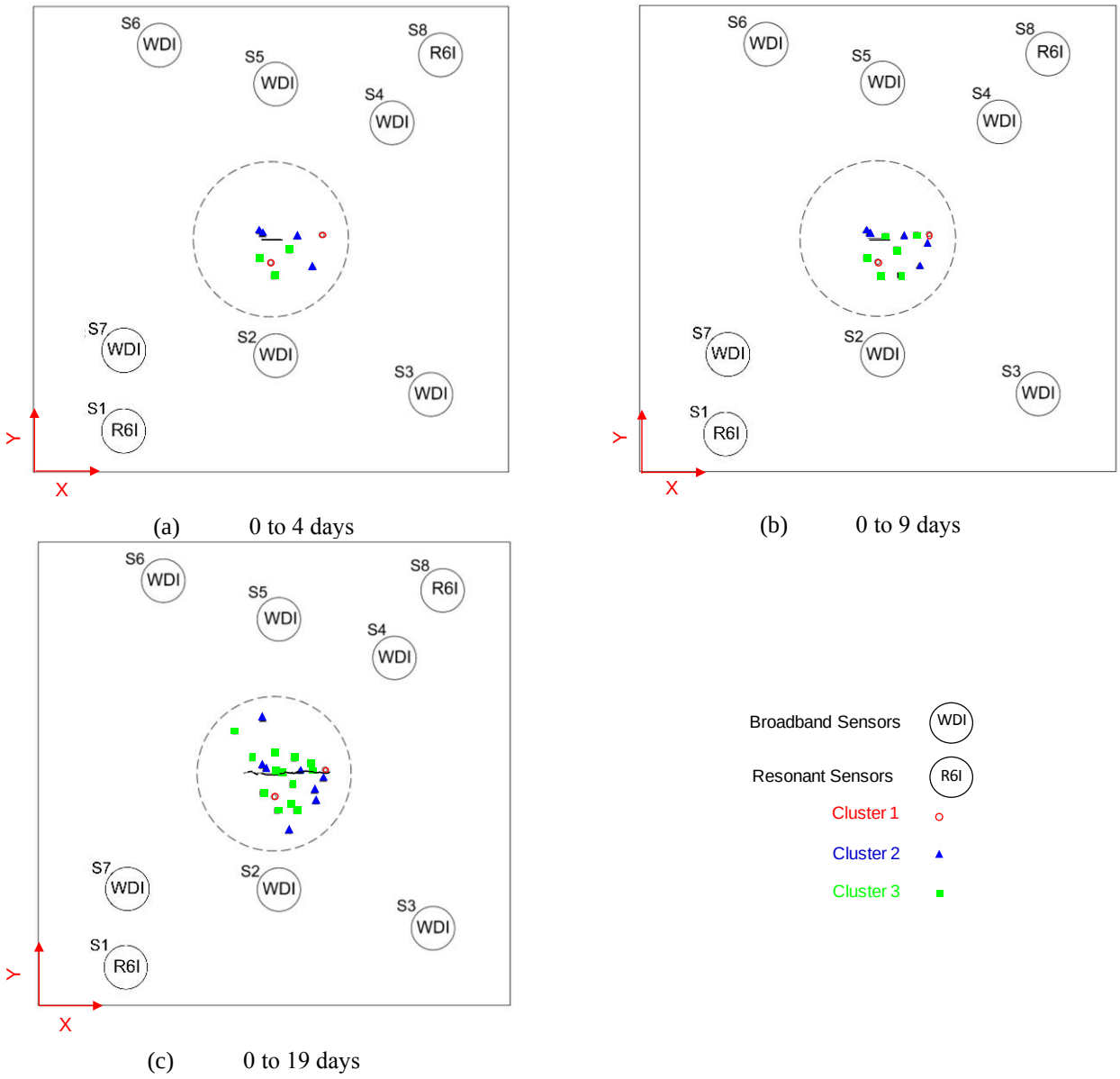

(a) 0 to 4 days

(b) 0 to 9 days

(c) 0 to 19 days

Fig. 14 Source location results

The signals in Cluster 2 have, on average, a larger energy concentration than other clusters for the frequencies less than 200 kHz as observed in Fig. 15b. The signals in Cluster 1, as mentioned before, have the largest energy concentration for the frequencies less than 100 kHz and almost uniform energy distribution in the other frequency ranges. Clusters 1 and 2 have much smaller AE energy contributions during the stress corrosion cracking process, and they include very weak signals. They can be mostly related to micro-crack formations and crack propagations.

4.2 Damage identification using b-value analysis

As mentioned in section 3.5, two b-values were calculated in this study; Incremental b-value and Global b-value. For the Incremental b-value, the b-values were calculated for each 30 hits. The global values were calculated based on the data up to 3, 5, 8, 9, 10, 12, and 19 days to include the entire time of the experiment and match the times attributed to the Incremental b-values. The results are shown in Fig. 16. In both methods, an occurrence of the first visible crack can be observed to be associated with the minimum b-value. Incremental b-values after the first visible crack are larger than the values before the first visible crack and do not consider the cumulative characteristic of damage. However, Global b-values separates the SCC process into two regions; before the visible crack and after the visible crack (Fig. 16b). This parameter seems to be more reliable than the Incremental b-value for damage identification and quantification of the steel plate affected by SCC.

Coefficients of determination or R^2-values were calculated using Eq. 5 for all calculated Global b-values and are presented in Fig. 17. There is a clear trend in the calculated R^2-values in terms of time. Before the first visible crack, the coefficients of determination are

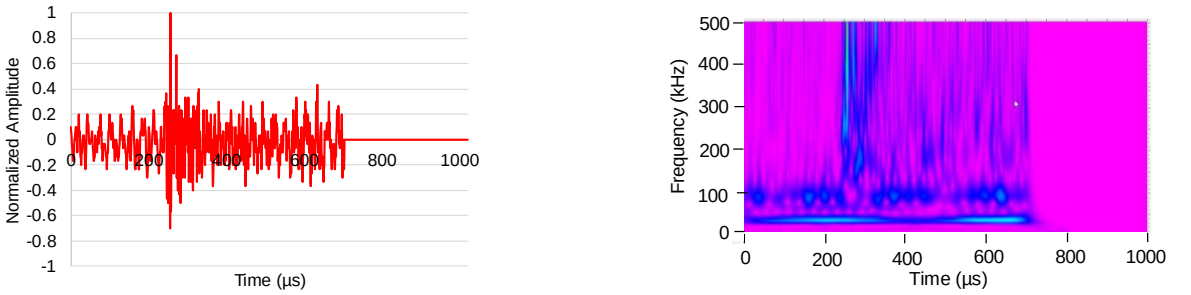

(a) Cluster 1

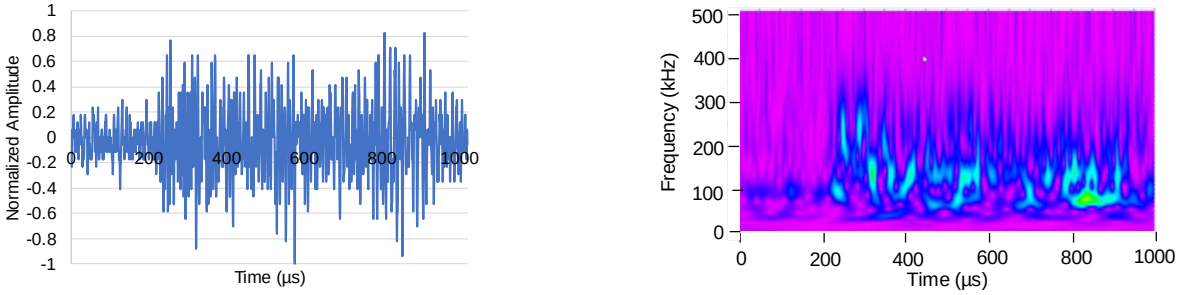

(b) Cluster 2

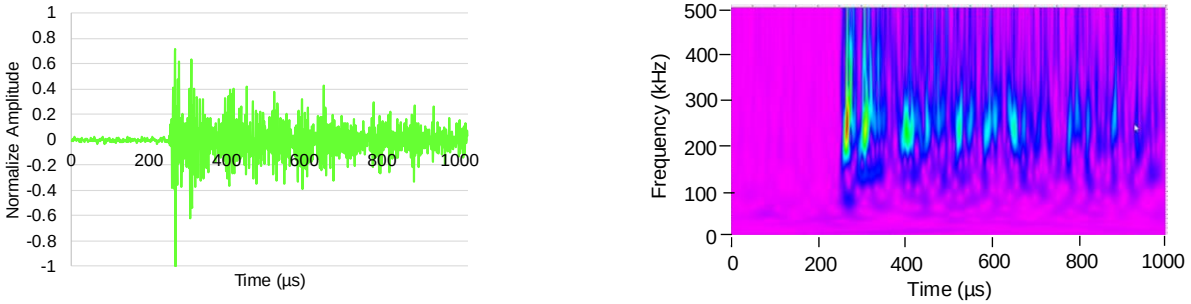

(c) Cluster 3

Fig. 15 Waveforms and wavelet contours for clusters

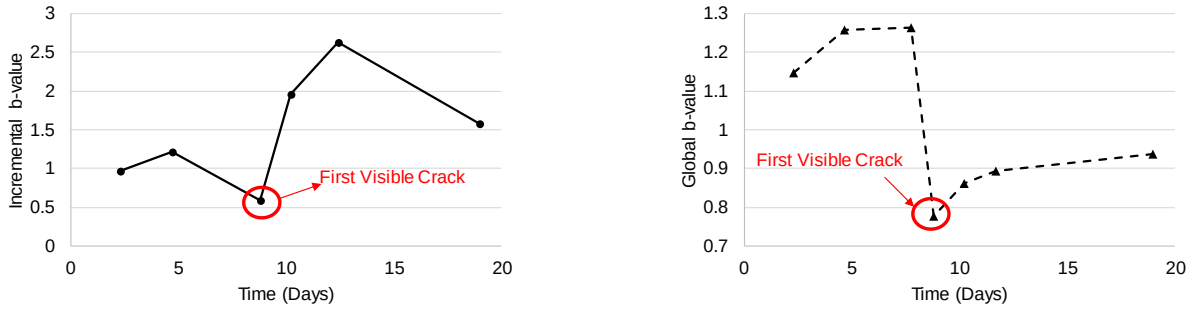

(a) (b)

Fig. 16 b-value results. (a) Incremental b-value; (b) Global b-value

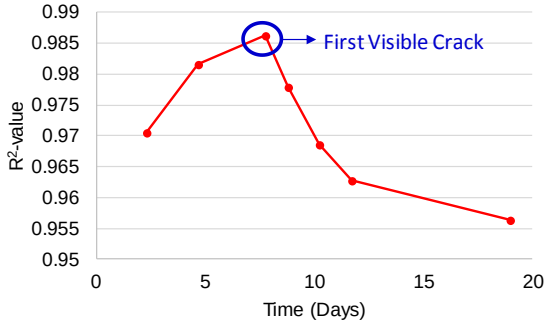

Fig. 17 R^2-value calculated for Global b-values

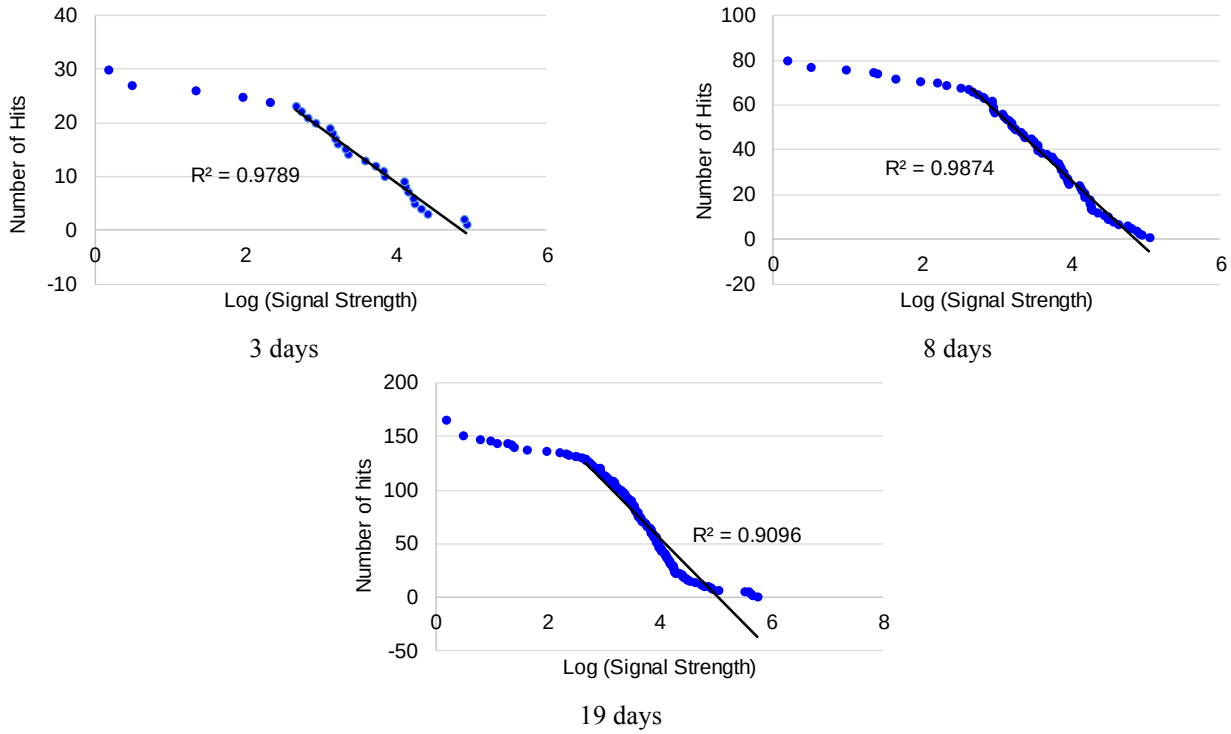

Fig. 18 Linear regression of Log (Signal Strength) versus N distributions for different experiment times

increasing because a larger amount of data was generated and made the coefficients of determination closer to linearity. At the first visible crack, AE events with larger amplitudes were generated, which were outliers from the previous AE data. These outliers caused the amplitude (*A*) versus *logN* to become farther from the linear relationship. This change in the coefficients of determination can be observed in Fig. 17 after the first visible crack. The change rate is larger around the first visible crack and then decreases as the SCC continues.

The b-value was modified to be used for signal strength instead of amplitude. The relationship between *log(Signal Strength)* versus *N* is used to conduct linear regression and the AE data up to the desired time was considered for calculation. The *log (Signal Strength)* versus *N* distributions are illustrated in Fig. 18 for 3, 8, and 19 days. As seen in Fig. 18, the relationship between *log(Signal Strength)* and *Number of hits* (N) are bilinear. Linear regression analysis was conducted on the second branch of the curves because the second branch is related to the stronger signals, which can be associated with the prominent damage in the plate. The R^2-values for 19 days are lower than the values before 8 days.

The variation of R^2-values in terms of experiment time is shown in Fig. 19. A similar trend, like that for Global b-value (Fig. 17), is observed in Fig. 19. The coefficients of determination increase to a point corresponding to 8 days and then decreases abruptly after this point, which can be related to the first visible crack. The decreasing rate in R^2-values after the first visible crack declines as the SCC continues. The calculated R^2-values based on the signal strength show a larger variation from the maximum to minimum than R^2-values based on the amplitude. Therefore, this index can also be utilized for damage identification and quantification.

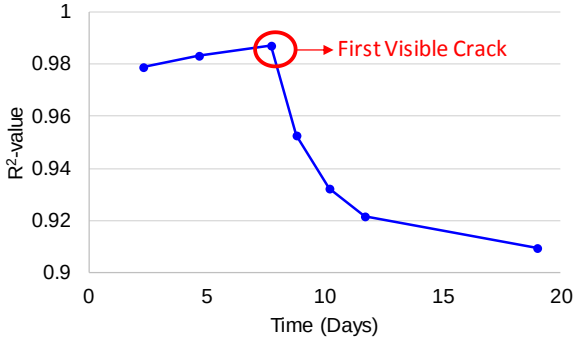

Fig. 19 R^2-value calculated for linear regression of Log (Signal Strength) versus number of hits

5. Conclusion

In this paper, the stress corrosion cracking (SCC) process of a steel plate was studied using AE. The frequency-energy based features were derived from the AE signals and utilized as an input matrix in an agglomerative hierarchical algorithm for an unsupervised clustering purpose. The clustered AE data were localized, and the signal signatures of the AE data associated with the damage in the steel plate were identified. Global and incremental b-value analyses were conducted for the identification of cracking stages. The main conclusions are as follows:

- Cluster 3 has the largest AE energy contribution during the experiment. Moreover, most of the located events are associated with Cluster 3. The signals in Cluster 3 can be attributed to the major damage due to SCC in the steel plate. Their frequency ranges concentrate mostly between 150-300 kHz.

- Global b-values calculated based on amplitude illustrate a more reliable method than incremental b-values for both identification and quantification of damage caused by SCC. Because Global b-values can identify both initiation of major damage and different stages (micro-stage and macro stage) of damage in the steel plate. In other words, the Global b-value index considers the cumulative characteristic of damage.
- The damage stages and progression in the steel plate caused by the stress corrosion cracking process are indicated by R^2-values calculated by conducting linear regression. This factor can also be used for damage identification and quantification caused by stress corrosion cracking.
- The relationship between *log(Signal Strength)* and the number of hits exceeding a desired Signal Strength value *(N)* is bilinear. A tale branch of the curve can be used for linear regression and calculating the R^2-values. A similar trend was achieved as the one for Global b-value. However, the variation of R^2-values calculated based on signal strength is higher than the R^2-values for Global b-values. Therefore, this index shows differences in the damage stages more clearly than the R^2-values of the Global b-value analysis. This index can also be utilized as a damage index for the identification and quantification of the defects due to SCC.

This research will continue to conduct a test on a full-scale steel plate, which resembles the real size of the dry storage system. Some conditions (limitation in the number of sensors and sensor locations) for structural health monitoring of large-scale structures such as the DCSSs are different than small-scale structures and therefore is the subject of future research.

Acknowledgments

This material is based upon work supported by Electric Power Research Institute (EPRI) under the project number 1-108781.

Data availability

The raw/processed data required to reproduce these findings cannot be shared at this time as the data also forms part of an ongoing study.

References

Ahmadi, H.R. and Anvari, D. (2018), "Health monitoring of pedestrian truss bridges using cone-shaped kernel distribution", *Smart Struct. Syst.*, **22**(6), 699-670. https://doi.org/10.12989/sss.2018.22.6.699.

Ahmadi, H.R., Daneshjoo, F. and Khaji, N. (2015), "New damage indices and algorithm based on square time–frequency distribution for damage detection in concrete piers of railroad bridges", *Struct. Control Health Monitor.*, **22**(1), 91-106. https://doi.org/10.1002/stc.1662.

Akaike, H. (1998), *Information Theory and an Extension of the Maximum Likelihood Principle*, Springer, Germany. https://doi.org/10.1007/978-1-4612-1694-0_15.

Alvarez, M., Lapitz, P. and Ruzzante, J. (2008), "AE response of type 304 stainless steel during stress corrosion crack propagation", *Corrosion Sci.,* **50**(12), 3382-3388. https://doi.org/10.1016/j.corsci.2008.08.028.

Bayat, M., Ahmadi, H. R., Kia, M. and Cao, M. (2019), "Probabilistic seismic demand of isolated straight concrete girder highway bridges using fragility functions", *Adv. Concrete Construct.*, **7**(3), 183-189. https://doi.org/10.12989/acc.2019.7.3.183.

Bayat, M., Ahmadi, H.R. and Mahdavi, N. (2019), "Application of power spectral density function for damage diagnosis of bridge piers" *Struct. Eng. Mech.*, **71**(1), 57-63. https://doi.org/10.12989/sem.2019.71.1.057

Calabrese, L., Campanella, G. and Proverbio, E. (2010), "Use of cluster analysis of acoustic emission signals evaluating damage severity in concrete structures ", *J. Acoustic Emission*, **28**.

Carpinteri, A., Xu, J., Lacidogna, G. and Manuello, A. (2012), "Reliable onset time determination and source location of acoustic emissions in concrete structures", *Cement Concrete Compos.*, **34**(4), 529-537, https://doi.org/10.1016/j.cemconcomp.2011.11.013.

Dastjerdi, P.B. and Ahmadi, M. (2018), "Characterizing the damage mechanisms in mode II delamination in glass/epoxy composite using acoustic emission", *Struct. Eng. Mech.*, **67**(5), 545-553. https://doi.org/10.12989/sem.2018.67.5.545

Dennis Jr, J.E. and Welsch, R.E. (1978), "Techniques for nonlinear least squares and robust regression", *Communications in Statistics-Simulation Computation*, **7**(4), 345-359. https://doi.org/10.1080/03610917808812083.

Du, G., Li, J., Wang, W., Jiang, C. and Song, S. (2011), "Detection and characterization of stress-corrosion cracking on 304 stainless steel by electrochemical noise and acoustic emission techniques", *Corrosion Sci.,* **53**(9), 2918-2926, https://doi.org/10.1016/j.corsci.2011.05.030.

Forde, M.C., Colombo, S., Main, I.G., Ohtsu, M. and Shigeishi, M. (2016), "Predicting the ultimate load capacity of concrete bridge beams from the 'Relaxation Ratio', analysis of AE signals", *Progress in Acoustic Emission*. **18**, 359-364.

Fregonese, M., Idrissi, H., Mazille, H., Renaud, L. and Cetre, Y. (2001), "Initiation and propagation steps in pitting corrosion of austenitic stainless steels: Monitoring by acoustic emission", *Corrosion Sci.,* **43**(4), 627-641, https://doi.org/10.1016/S0010-938X(00)00099-8.

Ge, M. (2003), "Analysis of source location algorithms: Part 2. Iterative methods", *J. Acoustic Emission*. **21**(1), 29-51.

Gholizadeh, S., Leman, Z. and Baharudin, B.T.H.T. (2015), "A review of the application of acoustic emission technique in engineering", *Struct. Eng. Mech.*, **54**(6), 1075-1095. https://doi.org/10.12989/sem.2015.54.6.1075

Hakan, G. (2008), "Application of continuous wavelet transform to detect damage in thin-walled beams coupled in bending and torsion", *Struct. Eng. Mech.*, **29**(3), 351-354. https://doi.org/10.12989/sem.2008.29.3.351.

Hill, J.W. (2018), *Acoustic Emission Detection in 304h Stainless Steel Due to Intergranular Stress Corrosion Cracking*, University of South Carolina.

Holford, K.M., Davies, A., Pullin, R. and Carter, D. (2001), "Damage location in steel bridges by acoustic emission", *J. Intelligent Mater. Syst. Struct.*, **12**(8), 567-576, 10.1177/10453890122145311.

Hsu, N. (1981), "Characterization and calibration of acoustic emission sensors", *Material Evaluation*, **39**, 60-68.

Hwang, W., Bae, S., Kim, J., Kang, S., Kwag, N. and Lee, B. (2015), "Acoustic emission characteristics of stress corrosion cracks in a type 304 stainless steel tube", *Nuclear Eng., Technol.,*

47(4), 454-460. https://doi.org/10.1016/j.net.2015.04.001.

Jirarungsatian, C. and Prateepasen, A. (2010), "Pitting and uniform corrosion source recognition using acoustic emission parameters", *Corrosion Sci.,* **52**(1), 187-197, https://doi.org/10.1016/j.corsci.2009.09.001.

Kainuma, S., Yamamoto, Y., Ahn, J.H. and Jeong, Y.S. (2018), "Evaluation method for time-dependent corrosion depth of uncoated weathering steel using thickness of corrosion product layer", *Struct. Eng. Mech.*, **65**(2), 191-201. https://doi.org/10.12989/sem.2018.65.2.191

Khorshidi, N., Ansari, M. and Bayat, M. (2014), "An investigation of water magnetization and its influence on some concrete specificities like fluidity and compressive strength", *Comput. Concrete*, **13**(5), 649-657.https://doi.org/10.12989/cac.2014.13.5.649.

Kim, Y.P., Fregonese, M., Mazille, H., Féron, D. and Santarini, G. (2003), "Ability of acoustic emission technique for detection and monitoring of crevice corrosion on 304L austenitic stainless steel", *Ndt E.,* **36**(8), 553-562, https://doi.org/10.1016/S0963-8695(03)00065-3.

Kovač, J., Legat, A., Zajec, B., Kosec, T. and Govekar, E. (2015), "Detection and characterization of stainless steel SCC by the analysis of crack related acoustic emission", *Ultrasonics*, **62**, 312-322, 10.1016/j.ultras.2015.06.005.

Lee, C., Scholey, J., Worthington, S., Wilcox, P., Wisnom, M., Friswell, M. and Drinkwater, B. (2008), "Acoustic emission from pitting corrosion in stressed stainless steel plate", *Corrosion Eng. Sci. Technol.*, **43**(1), 54-63, https://doi.org/10.1179/174327808X286176.

Maeda, N. (1985), "A method for reading and checking phase times in autoprocessing system of seismic wave data", *J. Seismological Soc.*, **38**, 365-379, https://doi.org/10.4294/zisin1948.38.3_365.

Mahdavi, N., Ahmadi, H. R. and Bayat, M. (2019), "Efficient parameters to predict the nonlinear behavior of FRP retrofitted RC columns", *Struct. Eng. Mech.*, **70**(6), 703-710. https://doi.org/10.12989/sem.2019.70.6.703.

Mazille, H., Rothea, R. and Tronel, C. (1995), "An acoustic emission technique for monitoring pitting corrosion of austenitic stainless steels", *Corrosion Sci.,* **37**(9), 1365-1375, https://doi.org/10.1016/0010-938X(95)00036-J.

Mirfakhraei, S.F., Ahmadi, H.R. and Chan, R. (2020), "Numerical and experimental research on actuator forces in toggled active vibration control system (Part I: Numerical)", *Smart Struct. Syst.*, **25**(2), 229. https://doi.org/10.12989/sss.2020.25.2.229.

Mistras Group (2014), *Express-8 AE System User Manual*, Princeton Junction, NJ, USA.

Mistras Group (2011a), *WDI-AST Sensor Wideband Integral Preamplifier Sensor*, P. A. Corporation, Princeton Junction, NJ, USA.

Mistras Group (2011b), *R6i-AT Integral Preamplifier Resonant Sensor*, P. A. Corporation, Princeton Junction, NJ, USA.

Morizet, N., Godin, N., Tang, J., Maillet, E., Fregonese, M. and Normand, B. (2016), "Classification of acoustic emission signals using wavelets and Random Forests: Application to localized corrosion", *Mech. Syst. Signal Processing*, **70**, 1026-1037. https://doi.org/10.1016/j.ymssp.2015.09.025.

Murtagh, F. and Legendre, P. (2014), "Ward's hierarchical agglomerative clustering method: which algorithms implement Ward's criterion?", *J. Classification*, **31**(3), 274-295, https://doi.org/10.1007/s00357-014-9161-z.

Rao, M. and Lakshmi, K.P. (2005), "Analysis of b-value and improved b-value of acoustic emissions accompanying rock fracture", *Current Sci.*, 1577-1582.

Roberts, T. and Talebzadeh, M. (2003), "Fatigue life prediction based on crack propagation and acoustic emission count rates", *J. Construct. Steel Res.*, **59**(6), 679-694, https://doi.org/10.1016/S0143-974X(02)00065-2.

Shaikh, H., Amirthalingam, R., Anita, T., Sivaibharasi, N., Jaykumar, T., Manohar, P. and Khatak, H. (2007), "Evaluation of stress corrosion cracking phenomenon in an AISI type 316LN stainless steel using acoustic emission technique", *Corrosion Sci.,* **49**(2), 740-765, https://doi.org/10.1016/j.corsci.2006.06.007.

Soltangharaei, V., Anay, R., Assi, L., Ziehl, P. and Matta, F. (2018), "Damage identification in cement paste amended with carbon nanotubes", *AIP Conference Proceedings* https://doi.org/10.1063/1.5031529.

Soltangharaei, V., Anay, R., Hayes, N., Assi, L., Le Pape, Y., Ma, Z. and Ziehl, P. (2018), "Damage mechanism evaluation of large-scale concrete structures affected by alkali-silica reaction using acoustic emission", *Appl. Sci.*, **8**(11), 2148, https://doi.org/10.3390/app8112148.

Suzuki, H., Kinjo, T., Hayashi, Y., Takemoto, M., Ono, K. and Hayashi, Y. (1996), "Wavelet transform of acoustic emission signals", *J. Acoustic Emission*, **14**, 69-84.

Tan, P.-N., Steinbach, M. and Kumar, V. (2018), *Data Mining Cluster Analysis: Basic Concepts and Algorithms*, Pearson Addison-Wesley, India.

Wu, K., Lee, S., Lee, W.S., Hong, D.P. and Byeon, J.W. (2015), "Corrosion damage monitoring of stainless steel by acoustic emission", *New Developments Mech. Mech. Eng.*, Vienna, Austria.

Xu, J., Han, E.H. and Wu, X. (2012), "Acoustic emission response of 304 stainless steel during constant load test in high temperature aqueous environment", *Corrosion Sci.,* **63**, 91-99, https://doi.org/10.1016/j.corsci.2012.05.021.

Xu, J., Wu, X. and Han, E.H. (2011), "Acoustic emission during pitting corrosion of 304 stainless steel", *Corrosion Sci.,* **53**(4), 1537-1546, https://doi.org/10.1016/j.corsci.2011.01.030.

Xu, J., Wu, X. and Han, E.H. (2013), "Acoustic emission response of sensitized 304 stainless steel during intergranular corrosion and stress corrosion cracking", *Corrosion Sci.,* **73**, 262-273, https://doi.org/10.1016/j.corsci.2013.04.014.

Yu, J., Ziehl, P., Zárate, B. and Caicedo, J. (2011), "Prediction of fatigue crack growth in steel bridge components using acoustic emission", *J. Construct. Steel Res.,* **67**(8), 1254-1260, https://doi.org/10.1016/j.jcsr.2011.03.005.

CC